Hypersonic Drag, Stability, and Wake Data for Cones and Spheres

W. C. Lyons Jr.,* J. J. Brady,† and Z. J. Levensteins‡
U. S. Naval Ordnance Laboratory, White Oak, Silver Spring, Md.

Tests have been conducted in the Naval Ordnance Laboratory's ballistics ranges to investigate the drag, stability, and wake characteristics of slender cones and spheres at very high speeds. Drag coefficients were found to be linear functions of the mean squared angle of attack. Zero angle of attack drag coefficients were correlated using a mean viscous interaction parameter. Stability derivatives were found to be independent of the mean squared angle of attack. Good agreement was obtained between the experimentally determined drag and stability coefficients and theory. The width of the turbulent viscous core behind both cones and spheres was found to be proportional to the cube root of (xC_DA). The constant of proportionality was the same for cones and spheres and varied with flight Mach number. Wake transition Reynolds numbers were found to be independent of the freestream body Reynolds number for a constant Mach number, but strongly dependent on flight Mach number.

Nomenclature

A = base area
C = Chapman viscosity constant
C_D = drag coefficient
C_{D_0} = drag coefficient at zero angle of attack
C_{DB} = base drag coefficient
C_{DF} = friction drag coefficient
C_{DP} = pressure drag coefficient
$\Delta C_{DF(ip)}$ = friction drag increase due to induced pressure
$\Delta C_{DF(tc)}$ = friction drag increase due to transverse curvature
$\Delta C_{DP(ip)}$ = pressure drag increase due to induced pressure
C_f = local skin-friction coefficient (referenced to local dynamic pressure)
$C_{L\alpha}$ = slope of the lift force coefficient
$C_{M\alpha}$ = slope of the pitching moment coefficient
$C_{M_q} + C_{M\dot{\alpha}}$ = damping moment coefficient
$C_{N\alpha}$ = slope of the normal force coefficient
c.g. = center of gravity location measured from nose
c.p. = center of pressure location measured from nose
d = base diameter
I = transverse moment of inertia
k = defined in Eq. (3)
L = length of model
m = mass of model
M = Mach number
P = static pressure
r_B = base radius
r_N = nose radius
R_{e_θ} = local flow Reynolds number based on boundary-layer momentum thickness
R_{∞_s} = freestream Reynolds number based on arc length
$R_{\infty_{x_1}}$ = incipient wake transition Reynolds number based on freestream conditions
$R_{\infty_{x_2}}$ = fully turbulent wake transition Reynolds number based on freestream conditions
S = total wetted area
T = absolute temperature
V = velocity
x = downstream distance measured from base of model
x_1 = distance to incipient transition measured from base of model
x_2 = distance to fully turbulent transition measured from base of model
α = angle of attack
$\bar{\alpha}^2$ = mean squared angle of attack
γ = ratio of specific heats
δ = diameter of turbulent core of wake
θ_c = cone half angle
μ = viscosity
ρ = density
$\bar{\chi}$ = viscous interaction parameter
$\bar{\chi}_M$ = mean viscous interaction parameter [see Eq. (2)]

Subscripts

c = inviscid sharp-nosed cone surface conditions
e = local conditions just outside the boundary layer
∞ = ambient range conditions

Presented as Preprint 64-44 at the AIAA Aerospace Sciences Meeting, New York, January 20–22, 1964; revision received July 27, 1964. The authors would like to acknowledge the support and many helpful suggestions contributed during this program by R. E. Wilson, Associated Technical Director for Aeroballistics at the Naval Ordnance Laboratory.

* Chief, Missile Dynamics Division. Member AIAA.
† Supervisory Aerospace Engineer.
‡ Supervisory Research Aerospace Engineer. Member AIAA.

Introduction

With vehicles flying at very high speeds and high altitudes, a high Mach number, low Reynolds number flow regime exists which is of considerable interest. It is well known that, at high Mach numbers and low Reynolds numbers, the laminar boundary layer can become very thick. In fact, for slender cones flying at hypersonic Mach numbers, the boundary-layer thickness can be the same order of magnitude as the radius of the cone. The thick boundary layer can significantly alter the inviscid flow field about the body. This phenomenon has been described by Hayes[1] and Probstein.[1, 2] Since boundary-layer characteristics are dependent upon inviscid flow field characteristics, an interaction between the two regions exists. Pressures are induced in the inviscid flow field which can affect both the aerodynamic drag and the stability characteristics of the body. Transverse curvature effects can significantly increase the skin-friction drag on the body. Theoretical analyses of transverse curvature and induced pressure effects due to thick boundary layers on slender bodies have been presented by a number of authors.[2–4]

Experimental results of force and moment tests on slender cones in hypersonic wind tunnels have recently been reported.[5, 6] Zero-lift drag coefficients were correlated by Whitfield and Griffith[6] using a freestream viscous parameter defined as $M_\infty(C_\infty/R_{\infty_s})^{1/2}$.

Table 1 Test conditions for drag and stability data

Shot	r_B	Test gas	P_∞, mm Hg	T_∞, °R	V_∞, fps	M_∞	$R_{\infty_s} \times 10^{-6}$	$\bar{\chi}_M$	$\frac{M_\infty}{(R_{\infty_s})^{1/2}}$
4885	0.2	air	100.3	533	14,730	12.96	1.355	0.514	0.0111
4897	↑	N_2	98.8	533	14,940	12.92	1.368	0.517	0.0128
4901		↑	21.4	531	15,280	13.24	0.303	1.292	0.0241
4910			61.0	533	13,760	11.90	0.778	0.634	0.0135
4912			63.4	533	14,180	12.27	0.833	0.639	0.0134
4913			21.9	531	14,300	12.39	0.291	1.187	0.0230
4916			60.5	533	15,110	13.07	0.848	0.700	0.0142
4917		↓	100.9	534	14,930	12.90	1.396	0.511	0.0118
4918		N_2	20.5	532	15,100	13.06	0.287	1.306	0.0244
4937		air	24.6	535	14,950	13.13	0.328	1.188	0.0229
4939		N_2	26.2	534	14,500	12.74	0.352	1.108	0.0215
4943		↑	153.9	534	14,200	12.50	2.026	0.386	0.0088
4951		↓	274.1	535	14,410	12.65	3.661	0.276	0.0066
4966		N_2	94.5	539	12,530	10.96	1.098	0.455	0.0105
268		air	5.08	514	16,810	15.06	0.084	3.218	0.0519
276		↑	5.54	517	16,670	14.89	0.087	3.047	0.0505
277			5.54	517	17,000	15.19	0.091	3.106	0.0503
279			5.59	517	16,870	15.07	0.091	3.069	0.0499
281			5.00	519	17,270	15.40	0.084	3.344	0.0531
282			5.21	519	17,180	15.32	0.084	3.251	0.0528
284			197.5	519	16,340	14.57	3.090	0.373	0.0083
286			5.21	521	18,320	16.30	0.091	3.464	0.0540
287			5.13	521	18,200	16.19	0.087	3.475	0.0549
299			5.23	527	14,740	13.04	0.073	2.775	0.0483
301	0.2		4.93	529	18,280	16.14	0.084	3.584	0.0556
306	0.5		140.2	531	12,930	11.39	4.204	0.214	0.0056
308	0.5		147.1	532	13,320	11.73	4.540	0.214	0.0055
310	0.5		149.6	536	14,700	12.90	5.028	0.232	0.0058
319	0.2	↓	4.83	533	17,290	15.21	0.077	3.443	0.0548
322	0.2	air	4.76	532	17,100	15.05	0.074	3.429	0.0553

The data being reported here are from free-flight ballistics range tests of slender cones. These tests, ranging in free-stream Mach number from approximately 12 to 16, were conducted at true velocities and therefore represent conditions of extremely high heat-transfer rates.

Because of the current importance and interest in wake flows, data on the growth of the viscous core of the wake and on the location of transition from laminar to turbulent flow in the wake are presented.

Description of Tests

Tests have been conducted in the Naval Ordnance Laboratory's (NOL) Pressurized Ballistics Range No. 3 and Hyperballistics Range No. 4 for the purpose of investigating the drag, stability, and wake characteristics of slender cones. These facilities are described in Ref. 8. The models used for these tests were 8° half-angle cones with nose to base radius ratios of 0.035. A sketch of this model is shown in Fig. 1. Wake characteristics are also presented for a 6.3° half-angle cone with a nose to base radius ratio of 0.03 and for spheres. Model sizes are listed in Tables 1 and 2. Drag and stability characteristics from the NOL free-flight tests of the 6.3° half-angle cones have been previously reported.[7]

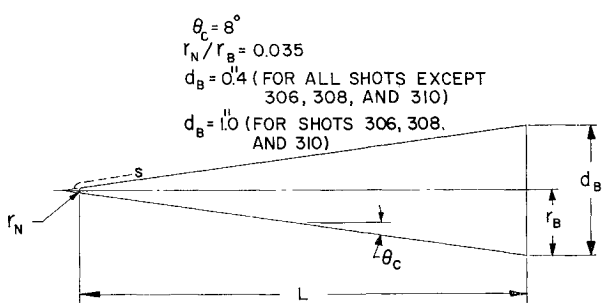

Fig. 1 Model configuration and nomenclature.

A list of the test conditions for the 8° and the 6.3° half-angle cone tests is presented in Tables 1 and 2. The sphere firings were made at velocities of approximately 16,500 fps and at ambient range pressures from 40 to 200 mm Hg. The average ambient range temperatures for these tests varied between 514° and 538°R with the Hyperballistics Range No. 4 generally having the lower temperatures. It was assumed that the wall temperature of the models did not vary significantly during the very short flight times.

These drag, stability, and wake data were obtained using spark shadowgraph instrumentation. Figure 2 is a spark shadowgraph photograph from shot 4951.

Drag and Stability Data

Data Reduction

The ballistics range technique for determining drag and static and dynamic forces and moments consists of fitting an appropriate equation to the accurately determined position coordinates of the model measured at discrete points along its trajectory. The six-position coordinates are obtained from orthogonal spark shadowgraph stations located at prescribed points in the range. The time of spark triggering for each of the stations is recorded on a chronograph. A description of the range data reduction techniques is given in Ref. 8. The values of the drag coefficients, their probable errors, and the mean squared angle of attack associated with each coefficient for the 8° cones are tabulated in Table 3. The

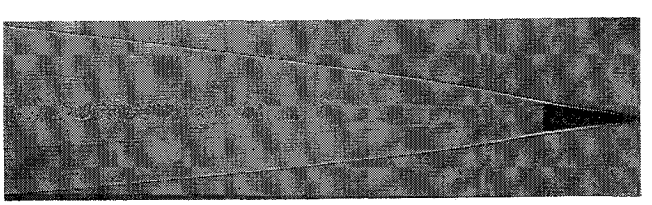

Fig. 2 Spark shadowgraph photograph from shot 4951.

Table 2 Wake transition data

Shot	θ_0, deg	r_N/r_B	d, in.	P_∞, mm Hg	M_∞	$R_{\infty d}$ × 10^{-6}	x_1/d	x_2/d	$R_{\infty x1}$ × 10^{-6}	$R_{\infty x2}$ × 10^{-6}
4302	6.3	0.03	0.222	85.8	9.04	0.128	18.50	...	2.38	...
4307	↑	↑	↑	98.5	8.21	0.134	9.45	15.20	1.27	2.05
4309				63.2	9.34	0.098	16.10	...	1.57	...
4335				50.7	9.14	0.076	21.4	...	1.63	...
4336				82.9	9.08	0.124	13.96	19.92	1.73	2.46
4337				100.2	9.13	0.152	8.11	17.76	1.32	2.70
4338			↓	76.4	9.13	0.114	15.25	...	1.74	...
4339			0.444	97.8	9.26	0.310	5.14	8.93	1.59	2.77
4400			0.222	56.2	9.13	0.084	21.5	...	1.80	...
4401			↑	62.4	9.04	0.092	25.6	...	2.25	...
4402				37.7	9.20	0.057	21.4	...	1.25	...
4299	↓	↓	↓	77.1	9.17	0.117	20.20	...	2.5	...
4296	6.3	0.03	0.222	99.9	9.00	0.152	7.39	15.41	1.122	2.34
4885	8.0	0.035	0.400	100.3	12.96	0.390	7.38	16.74	2.88	6.53
4897	↑	↑	↑	98.8	12.92	0.384	6.60	...	2.53	...
4916				60.5	13.07	0.238	12.5	...	2.98	...
4917				100.9	12.90	0.392	5.74	13.05	2.25	5.45
4939				26.2	12.74	0.100	32.50	...	3.25	...
4943			↓	153.9	12.50	0.576	6.00	11.60	3.46	6.68
4951			0.400	274.1	12.65	1.030	3.25	7.41	3.35	7.63
5030			0.800	192.4	6.67	0.767	1.10	...	0.844	...
5032			0.800	66.0	8.63	0.340	4.44	6.50	1.51	2.21
5045			0.800	81.4	9.48	0.465	3.16	...	1.47	...
284			0.400	197.5	14.57	0.900	5.00	13.60	4.50	12.30
308	↓	↓	1.000	147.1	11.73	1.296	2.92	5.39	3.79	7.00
310	8.0	0.035	1.000	149.6	12.90	1.450	4.22	6.69	6.10	9.70

static and dynamic stability coefficients for the 8° cones together with their probable errors (P.E.) as well as the center of pressure locations are also included in Table 3.

Data Analysis

Effects resulting from the slight blunting of slender bodies have been discussed in the literature.[9] The local flow properties at the outer edge of the boundary layer, particularly the Mach number, deviate considerably from the inviscid sharp cone values. The zero angle of attack local flow properties (M_e, T_e) for the portion of the body from the nose tangent point to the base were computed for each shot. These computations were performed using an IBM-7090 and the method described in Ref. 10. This method takes into account the curved bow shockwave that exists for slightly blunted slender bodies and allows a variation in total pressure along the outer edge of the boundary layer on the conical portion of the body. It assumes, however, that the static pressure along this surface is constant and equal to the inviscid sharp nosed cone value. Figure 3 shows the computed local Mach number variation along the model for the conditions of shot 282.

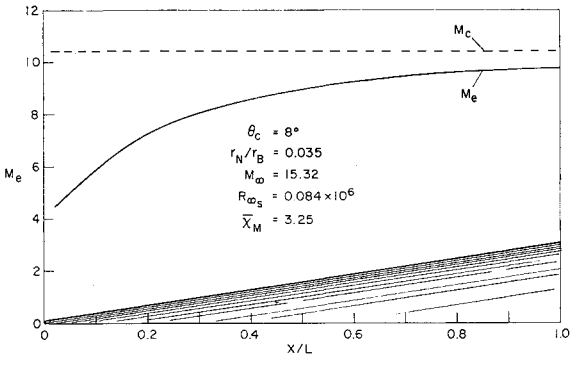

Fig. 3 Local Mach number distribution over a blunted cone for shot 282.

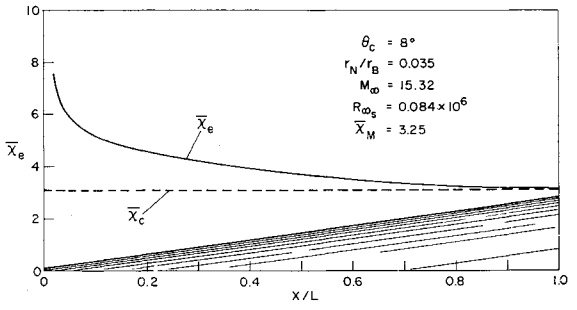

Fig. 4 Local viscous interaction parameter over a blunted cone for shot 282.

It has been shown that the viscous interaction effects between the boundary layer and the inviscid flow field are dependent on a viscous interaction parameter $\bar{\chi}$,[1] defined as

$$\bar{\chi} = M^3(C/R_e)^{1/2} \quad (1)$$

where C is the constant of proportionality in the linear viscosity-temperature relation suggested by Chapman.[11] It can be seen that $\bar{\chi}$ is strongly dependent on the Mach number. It was shown in Fig. 3 that the local Mach number M_e deviates considerably from the constant Mach number that would exist on a sharp nosed cone. It was therefore decided

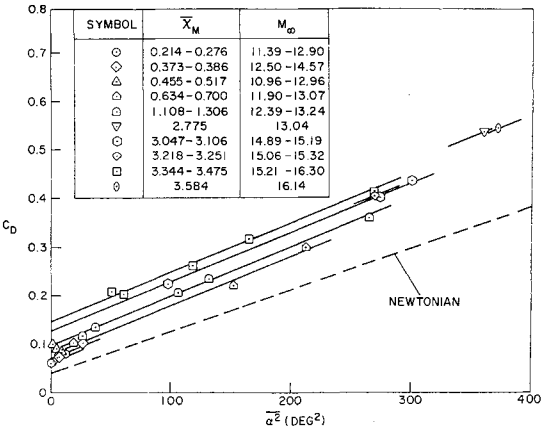

Fig. 5 Correlation of total drag coefficient with mean squared angle of attack.

to characterize the viscous effects on the aerodynamic data obtained from these tests by a mean viscous interaction parameter $\bar{\chi}_M$. This mean value of $\bar{\chi}_M$ was obtained by first computing local values of the interaction parameter $\bar{\chi}_e$ using the computed local properties. Values for $\bar{\chi}_M$ were then found numerically from the following equation:

$$\bar{\chi}_M = \frac{1}{S}\int_s \bar{\chi}_e d\sigma \qquad (2)$$

Values for $\bar{\chi}_M$ were computed for each shot and are listed in Tables 1 and 3. In Fig. 4, the distribution of $\bar{\chi}_e$ along the length of the cone is shown for shot 282.

Drag Data

The drag coefficients from these tests have been grouped according to the value of $\bar{\chi}_M$ which was computed for the particular shot. These drag coefficients have been plotted in Fig. 5 as a function of the mean squared angle of attack for the shot. Parallel straight lines have been faired through each $\bar{\chi}_M$ grouping of points. It can be seen from Fig. 5 that,

Table 3 Drag and stability data

Shot	4885	4897	4901	4910	4912	4913	4916	4917	4918	4937
Symbol	△	△	⌂	⌂	⌂	⌂	⌂	△	⌂	⌂
M_∞	12.96	12.92	13.24	11.90	12.27	12.39	13.07	12.90	13.06	13.13
$R_\infty \times 10^{-6}$	1.355	1.368	0.303	0.778	0.833	0.291	0.848	1.396	0.287	0.328
$\bar{\chi}_M$	0.514	0.517	1.292	0.634	0.639	1.187	0.700	0.511	1.306	1.188
$\overline{\alpha^2}$(deg)^2	2.4	9.5	106	213	153	266	19.0	9.8	27.0	132
P.E. (α)	0.0068	0.013	0.0035	0.018	...	0.016	0.0077	...	...	0.0052
P.E. (c.g.)	0.022	0.032	0.011	0.033	...	0.029	0.014	...	...	0.021
C_D	0.1010	0.0831	0.205	0.301	0.222	0.358	0.1016	0.087	0.0116	0.234
P.E.	0.0004	0.0006	0.002	0.002	0.002	0.008	0.0009	0.002	0.004	0.002
C_{D_0}	0.0986	0.0734	0.0969	0.0837	0.0659	0.0867	0.0822	0.0770	0.0885	0.099
$C_{L\alpha/\text{rad}}$	2.5	2.0	1.78	1.77	...	2.1	2.07	...	...	1.9
P.E.	1.1	0.5	0.04	0.08	...	0.1	0.09	...	...	0.1
$C_{N\alpha/\text{rad}}$	2.6	2.1	1.98	2.07	...	2.4	2.17	...	...	2.1
P.E.	1.1	0.5	0.04	0.08	...	0.1	0.09	...	...	0.1
$C_{M\alpha/\text{rad}}$	−0.94	−0.61	−0.526	−0.608	...	−0.595	−0.52	...	...	−0.544
P.E.	0.02	0.01	0.001	0.004	...	0.006	0.01	...	...	0.004
c.p./L	0.705	0.685	0.678	0.686	...	0.672	0.670	...	...	0.675
$C_{M_q} + C_{M\dot{\alpha}}$	...	−5.2	−9.3	−8.3	...	−11.4	−10.3	...	...	−5.0
P.E.	...	5.6	1.4	3.6	...	6.5	9.0	...	...	3.0

Shot	4939	4943	4951	4966	268	276	277	279	281	282
Symbol	⌂	◇	○	△	▽	⬡	⬡	⬡	□	▽
M_∞	12.74	12.50	12.65	10.96	15.06	14.89	15.19	15.07	15.40	15.32
$R_\infty \times 10^{-6}$	0.352	2.026	3.661	1.098	0.084	0.087	0.091	0.091	0.084	0.084
$\bar{\chi}_M$	1.108	0.386	0.276	0.455	3.218	3.047	3.106	3.069	3.344	3.251
$\overline{\alpha^2}$(deg)^2	37	7.3	0.6	5.8	318	98	301	275	166	270
P.E. (α)	0.0060	0.0096	0.0050	...	0.017	0.012	0.012	0.008	0.012	0.010
P.E. (c.g.)	0.018	0.017	0.007	...	0.040	0.050	0.040	0.035	0.050	0.043
C_D	0.134	0.0733	0.0638	0.0900	...	0.223	0.436	0.400	0.316	0.404
P.E.	0.002	0.0004	0.0003	0.008	...	0.002	0.002	0.005	0.002	0.002
C_{D_0}	0.096	0.0658	0.0632	0.084	...	0.123	0.129	0.120	0.147	0.129
$C_{L\alpha/\text{rad}}$	1.9	2.0	2.2	...	2.1	2.2	1.7	1.84	2.0	1.8
P.E.	0.2	0.3	0.5	...	0.2	0.2	0.1	0.09	0.2	0.1
$C_{N\alpha/\text{rad}}$	2.0	2.1	2.3	...	2.4	2.4	2.1	2.24	2.3	2.2
P.E.	0.2	0.3	0.5	...	0.2	0.2	0.1	0.09	0.2	0.1
$C_{M\alpha/\text{rad}}$	−0.574	−0.632	−0.860	...	−0.451	−0.554	−0.554	−0.511	−0.527	−0.532
P.E.	0.006	0.009	0.009	...	0.008	0.006	0.002	0.002	0.004	0.002
c.p./L	0.683	0.687	0.709	...	0.659	0.668	0.677	0.668	0.668	0.670
$C_{M_q} + C_{M\dot{\alpha}}$	−2.0	−6.2	...	...	...	...	−2	−10	−1.1	−10
P.E.	4.0	2.8	...	...	...	...	4	3	0.7	4

Shot	284	286	287	299	301	306	308	310	319	322
Symbol	◇	□	□	▽	◊	○	○	○	□	□
M_∞	14.57	16.30	16.19	13.04	16.14	11.39	11.73	12.90	15.21	15.05
$R_\infty \times 10^{-6}$	3.090	0.091	0.087	0.073	0.084	4.204	4.540	5.028	0.077	0.074
$\bar{\chi}_M$	0.373	3.464	3.475	2.775	3.584	0.214	0.214	0.232	3.443	3.429
$\overline{\alpha^2}$(deg)^2	26.7	61	270	361	373	12.3	6.0	0.2	51.2	119.4
P.E. (α)	...	0.009	0.012	0.020	0.010	0.010	...	...	0.015	0.024
P.E. (c.g.)	...	0.037	0.042	0.028	0.034	0.038	...	...	0.055	0.039
C_D	0.1028	0.204	0.414	0.536	0.546	0.0792	0.0734	0.0604	0.209	0.262
P.E.	0.0001	0.003	0.002	0.002	0.005	0.0004	0.0007	0.0004	0.002	0.004
C_{D_0}	0.0756	0.142	0.139	0.168	0.166	0.0666	0.0672	0.0602	0.157	0.140
$C_{L\alpha/\text{rad}}$	...	1.9	1.87	1.8	1.7	1.8	...	...	1.8	2.8
P.E.	...	0.2	0.09	0.2	0.1	0.2	...	...	0.5	0.3
$C_{N\alpha/\text{rad}}$	...	2.1	2.28	2.3	2.3	1.9	...	...	2.0	3.1
P.E.	...	0.2	0.09	0.2	0.1	0.2	...	...	0.5	0.3
$C_{M\alpha/\text{rad}}$	...	−0.550	−0.572	−0.61	−0.586	−0.420	...	...	−0.722	−0.47
P.E.	...	0.005	0.004	0.01	0.003	0.009	...	...	0.009	0.01
c.p./L	...	0.676	0.672	0.677	0.673	0.665	...	...	0.644	0.644
$C_{M_q} + C_{M\dot{\alpha}}$	...	...	−8	...	−7.0	−10	...	...	...	−11.0
P.E.	...	...	6	...	5.0	4	...	...	...	15.0

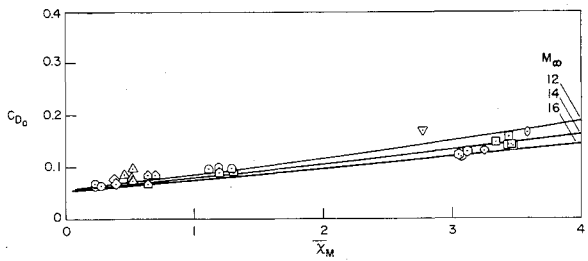

Fig. 6 Correlation of zero angle of attack drag coefficients with mean viscous interaction parameter.

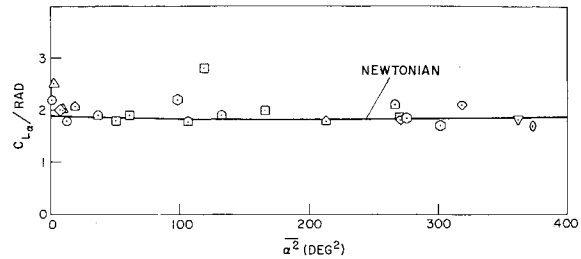

Fig. 8 Comparison of experimental values of C_{L_α} with Newtonian impact theory.

out of a total of 29 points, only 4 points deviated more than 5% from the straight line associated with a particular grouping. The slope k of these straight lines was used to reduce the drag coefficient measured for each shot to an equivalent zero angle of attack value using the equation

$$C_D = C_D - k\overline{\alpha^2} \tag{3}$$

Values of C_{D_0} for each shot are listed in Table 3.

In Fig. 6, the values of C_{D_0} are presented as a function of $\bar{\chi}_M$. The family of three curves also shown in this figure was theoretically computed. The theoretical values of C_{D_0} were obtained by summing six components of drag as follows: 1) inviscid pressure drag, C_{D_P}; 2) friction drag neglecting interaction effects, C_{D_F}; 3) increase in pressure drag due to induced pressure, $\Delta C_{D_{P(ip)}}$; 4) increase in friction drag due to induced pressure effects, $\Delta C_{D_{F(ip)}}$; 5) increase in friction drag due to transverse curvature effects, $\Delta C_{D_{F(tc)}}$; and 6) base drag, C_{D_B}.

The inviscid pressure drag coefficient was determined by assuming that inviscid cone pressure existed over the conical portion of the body. The component of the local force in the direction of the longitudinal axis of the body was integrated over the conical portion of the body and then referenced to freestream dynamic pressure and the base area of the body to obtain a drag coefficient. Using Newtonian impact theory, a drag coefficient was computed for the spherical nose cap again using freestream dynamic pressure and base area of the body as the reference. The sum of these two coefficients determined the inviscid pressure drag coefficient C_{D_P}.

The drag coefficient due to skin friction was obtained by first computing a local skin-friction coefficient for points along the body. The local force components in the direction of the longitudinal axis of the body were then integrated over the conical portion of the body and referenced to freestream dynamic pressure and base area. The local skin-friction coefficient was computed from equations given in Ref. 12 and presented in the form used here in Ref. 10 as

$$C_f = \frac{(0.644)^2}{R_{e_\theta}} \frac{T_e}{T'} \frac{\mu'}{\mu_e} \tag{4}$$

where

$$T'/T_e = 1 + 0.076(\gamma - 1)M_e^2 + 0.481[(T_w/T_e) - 1] \tag{5}$$

The increase in the pressure drag coefficient due to induced pressure and the increases in the friction drag coefficient due to induced pressure and transverse curvature were computed using the equations given by Probstein.[2] For the base drag coefficient, it was assumed that a vacuum existed at the base.

For the conditions at which these tests were conducted, the viscous interaction effects on the total drag coefficient were comparatively small. To illustrate the importance of the various drag components, a sample computation was made for a freestream Mach number and Reynolds number of 15.3 and 8.4 $\times$ 10^4, respectively. The results are presented in Table 4. The mean viscous interaction parameter for this computation was 3.25.

Reference 6 contains the only other hypersonic slender cone drag data available at conditions where viscous interaction effects were significant. Since it was shown in Ref. 6 that the drag coefficients could be correlated in terms of a freestream viscous parameter $M_\infty(C_\infty/R_{\infty_s})^{1/2}$, it was decided to also present the drag coefficients from these ballistics range tests as a function of this viscous parameter. Since it was assumed for these tests that the wall temperature was equal to the ambient range temperature, the constant C_∞ equaled unity. Figure 7 shows that these data also appear to correlate with this parameter

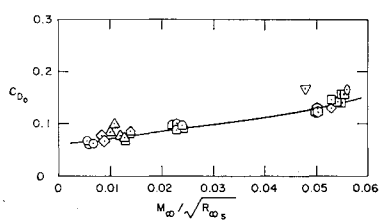

Fig. 7 Correlation of zero angle of attack drag coefficients with freestream viscous parameter.

Static Stability Data

The static stability derivatives and the center of pressure locations have been presented in Figs. 8–10 as a function of the mean squared angle of attack. Also presented for each of these parameters is a theoretically computed curve. These curves have been determined using Newtonian impact theory, and the computations were performed using the equations and tables in Ref. 13. The derivatives were obtained by computing the appropriate force or moment coefficients and then dividing them by the angles of attack for which they were computed. This is consistent with the linear assumption made in the ballistics range data reduction procedures.

Referring to Figs. 8–10, it is seen that there is no measurable variation in the derivatives or the center of pressure locations with angle of attack with the exception of data obtained at very small angles of attack. This indicates that the force and moment coefficients are linear over

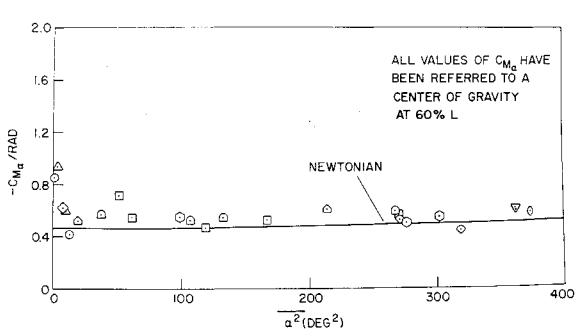

Fig. 9 Comparison of experimental values of C_{M_α} with Newtonian impact theory.

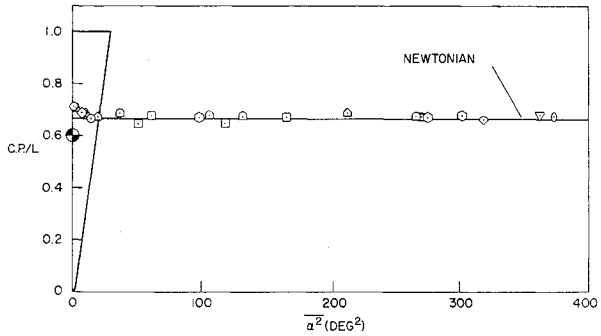

Fig. 10 Comparison of experimentally determined c.p. location with Newtonian impact theory.

most of the angle of attack range considered, which is the assumption made in the data reduction procedures used. Further, within the accuracy of these data, it was not possible to discern any viscous effects on these parameters, again with the possible exception of very small values of $\overline{\alpha^2}$. It is also noticed that the Newtonian impact theory, which neglects any viscous effects, can be used to predict these aerodynamic parameters. However, at very low angles of attack [below approximately 3° ($\overline{\alpha^2} < 10$)], there seems to be a slight increase in the experimental derivatives and a slight aft movement of the center of pressure location. It has been reported in Ref. 14 that experimentally measured pressure distributions over a slender cone at angle of attack could be predicted accurately using Newtonian impact theory except at small values of α. At angles of attack less than about 3°, Newtonian impact theory was not accurate for predicting the pressure. This is indicative of viscous effects altering the pressure distribution over slender cones at small angles of attack but becoming insignificant as the angle of attack increases. Since the stability derivatives are predominately pressure-dependent parameters, this trend of increasing values for the stability derivatives obtained in these current tests at very low angles of attack perhaps also reflects a viscous effect on these parameters.

Wake Flow Results

All of the experimental results presented in this section were obtained from measurements made on shadowgraph photographs of the wake flow. The shadowgraph instrumentation was sufficiently sensitive to record wake flow details behind the cones at an ambient range pressure of 20 mm Hg. However, behind spheres, the hypersonic wake flow was invisible by shadowgraph technique for about the first 200 diam downstream even at an ambient range pressure of 200 mm Hg. In this section are presented turbulent viscous core growth results for both cones and spheres and transition from laminar to turbulent flow results for cones. A sketch of the wake flow configuration and the pertinent nomenclature are shown in Fig. 11. For comparison, some results obtained at Massachusetts Institute of Technology/Lincoln and Avco/RAD ballistics ranges are presented.

Table 4 Computed drag coefficient components

Drag coefficient		Percent of total
C_{D_P}	0.0427	32.9
C_{D_F}	0.0643	49.5
$\Delta C_{D_{P(ip)}}$	0.0069	5.3
$\Delta C_{D_{F(ip)}}$	0.0037	2.8
$\Delta C_{D_{F(tc)}}$	0.0063	4.8
C_{D_B}	0.0061	4.7
$C_{D_{Total}}$	0.1300	100.0

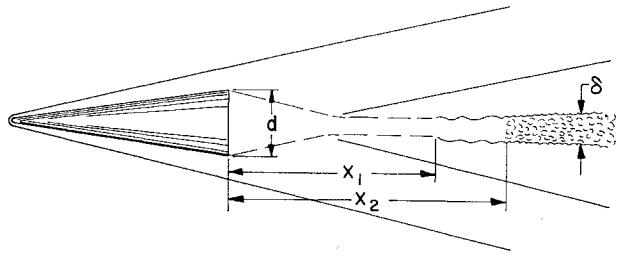

Fig. 11 Sketch of wake flow configuration.

Growth of Turbulent Core

The width of the turbulent core δ was determined from measurements made on a series of simultaneously exposed shadowgraph photographs of the wake. It was decided to record an average width for a 7-in. length of the turbulent core. The averaging was achieved by tracing the boundary of the shadowgraph of the turbulent core with a planimeter. Then the core width δ was obtained by dividing the planimeter reading by the 7-in. length.

Townsend[15] shows that for incompressible "self-preserving" turbulent wake flow the width of the viscous core δ is proportional to the cube root of $C_D A(x - x_0)$. C_D is the total drag coefficient of the body, A the area on which the drag coefficient is based, x the downstream distance behind the body, and x_0 is a virtual origin of the wake. In equation form, this can also be written as

$$\frac{\delta/d}{C_D{}^{1/3}} = K\left(\frac{x - x_0}{d}\right)^{1/3} \tag{6}$$

where d is the body diameter and K is a constant of proportionality. Following the incompressible results, an analysis of the NOL core growth data showed that the virtual origin x_0 was zero. A logarithmic plot of $(\delta/d)C_D{}^{-1/3}$ vs x/d of the NOL results for both spheres and cones is shown in Fig. 12. Also shown in the figure are the freestream Mach numbers M_∞ and freestream Reynolds numbers based on body diameter $R_{\infty d}$ at which the data were obtained. A constant drag coefficient of 0.9 was used for the spheres. The drag coefficients for the 8° half-angle cones were experimentally determined from ballistics range firings. From Fig. 12 it can be seen that the turbulent core growth in the wake region between 200 and 800 body diameters behind both spheres and cones is the same. For the Reynolds number variation in these experiments, there was no effect of this parameter on the development of the turbulent core. The equation of the curve that described the core growth for 20 to 800 body diameters behind cones and 200 to 800 body diameters behind spheres is

$$\frac{\delta/d}{C_D{}^{1/3}} = 0.9\left(\frac{x}{d}\right)^{1/3} \tag{7}$$

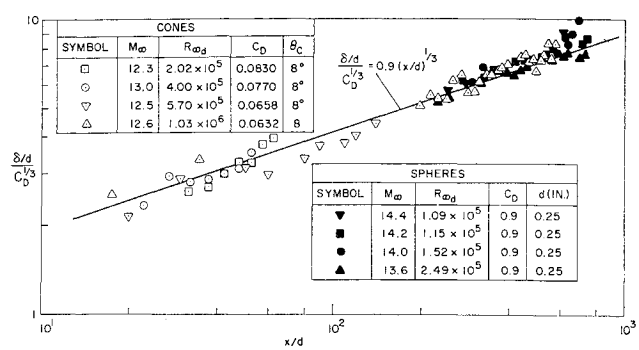

Fig. 12 Sphere and cone wake turbulent core growth results obtained in the NOL ballistics ranges.

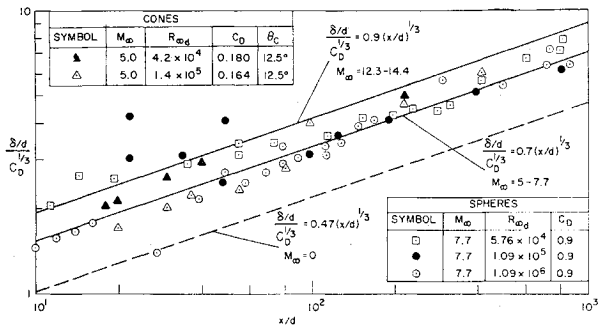

Fig. 13 Sphere and cone wake turbulent core growth results obtained in Lincoln Laboratory ballistics ranges and comparison of these results with NOL hypersonic and Townsend's incompressible results.

A similar correlation of cone and sphere turbulent core width data obtained by Slattery and Clay[16] is shown in Fig. 13. These data were obtained over a wide range of freestream Reynolds numbers. The freestream Mach numbers were 5 for the cones and 7.7 for the spheres. The turbulent core width was measured from a single schlieren photograph obtained during a shot. In order to present the Massachusetts Institute of Technology/Lincoln Laboratory data in a form suitable for analysis, a drag coefficient of 0.9 was assumed for the spheres. The drag coefficients for the 12.5° half-angle cones including pressure, skin friction, and base drag effects were theoretically computed. When x/d is less than 100, there is a great deal of scatter of the results. Also, in this region of the wake there appears to be a Reynolds number effect on the wake width. At the low Reynolds numbers, the core widths are greater than at the high ones. If the functional relationship of Eq. (6) and virtual origin x_0 equal to zero are assumed for these results, the constant of proportionality K that fits the results is 0.7. For comparison, Fig. 13 includes the following two other curves, the curve with $K = 0.9$ describing NOL results obtained at Mach numbers from $M_\infty = 12.3$ to 14.4, and the curve describing the turbulent core growth behavior of an incompressible wake. The latter one is Townsend's solution for the axisymmetric wake width,[15] where $K = 0.47$ was computed by letting the equilibrium flow constant $R_T = 14.1$ and the virtual origin of the wake x_0 again equal zero. A few core width data points from low supersonic Mach number sphere firings in NOL ballistics ranges also fall on Townsend's curve. These data points are not shown in Fig. 13. From the results shown in Fig. 13, it appears that the constant of proportionality K is a function of the flight Mach number. The constant of proportionality increases as the flight Mach number increases. A similar Mach number effect on the behavior of the hypersonic turbulent wake was found by Lykoudis[17] from theoretical considerations.

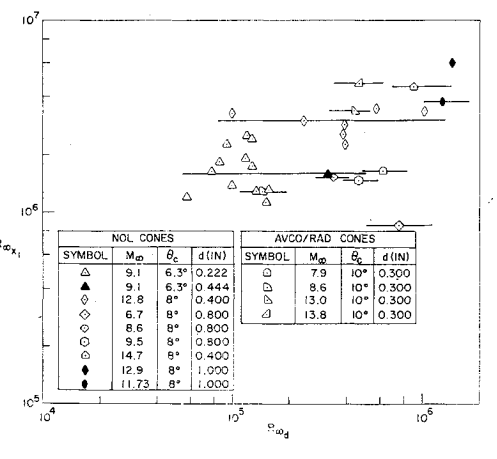

Fig. 14 Correlation of incipient wake transition Reynolds number.

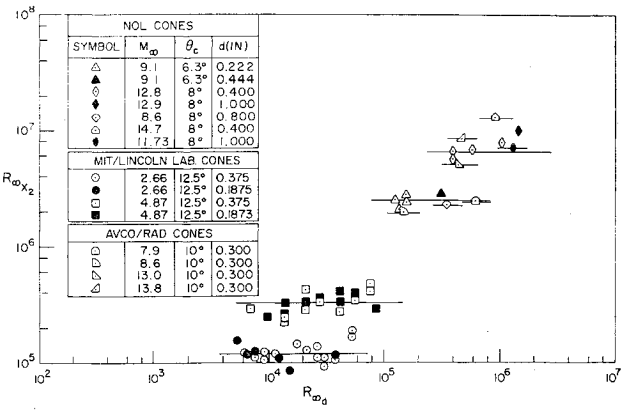

Fig. 15 Correlation of fully turbulent wake transition Reynolds number.

Transition from Laminar to Turbulent Flow in the Cone Wake

The length of laminar flow in the viscous core of the wake was measured on shadowgraph photographs obtained from hypervelocity firings of 6.3° and 8° half-angle cones. Figure 2 is a shadowgraph of an 8° half-angle cone wake at $M_\infty = 13$ and ambient range pressure $P_\infty = 100$ mm Hg. There were two length measurements made: x_1, the distance from the cone to the first appearance of instability in the laminar flow of the viscous core, and x_2, the distance from the cone to where the flow in the viscous core appears to have become fully turbulent. The test conditions, the measured x_1 and x_2 distances, and the wake transition Reynolds numbers are listed in Table 2.

Both the x_1, the incipient transition data and x_2, the fully turbulent transition data were correlated by forming the wake transition Reynolds numbers $R_{\infty_{x_1}}$ and $R_{\infty_{x_2}}$, respectively, and plotting them vs the freestream body Reynolds number R_{∞_d}. Figure 14 shows the incipient transition Reynolds number results. The solid symbol in the $\theta_c = 6.3°$ cone results represents a cone with a base diameter of 0.444 in. The open symbols are for 0.222 in. base diameter cones. The base diameters for the 8° half-angle cones were 0.400, 0.800, and 1.000 in. Thus, the variation in the body Reynolds number was obtained by both ambient range pressure and base diameter variations. The two solid symbols in the 8° half-angle 1.000-in. base diameter cone results are for data obtained in the Hyperballistics Range No. 4. Because of the smaller size of the shadowgraph photographs in this ballistics range facility, the two data points are considered less reliable than the data obtained in the Pressurized Ballistics Range No. 3. Therefore, it is not certain whether the high values of the wake transition Reynolds number show a body scale effect or merely poorly determined data. Also included in Fig. 14 are some incipient transition results for 10° half-angle cones obtained at various freestream Mach numbers and Reynolds numbers in the Avco/Rad ballistics ranges.[18]

Figure 15 is a similar correlation of the fully turbulent transition Reynolds number results. In addition to the NOL and Avco/RAD results, there are also shown transition results obtained by Slattery and Clay in the Massachusetts Institute of Technology/Lincoln Laboratory's ballistics ranges.[16] The open symbols represent 0.375 in., the solid symbols 0.1875 in. base diameter 12.5° half-angle cones. Both Avco/RAD and Lincoln Laboratory transition data were obtained from measurements made on schlieren photographs of the wake.

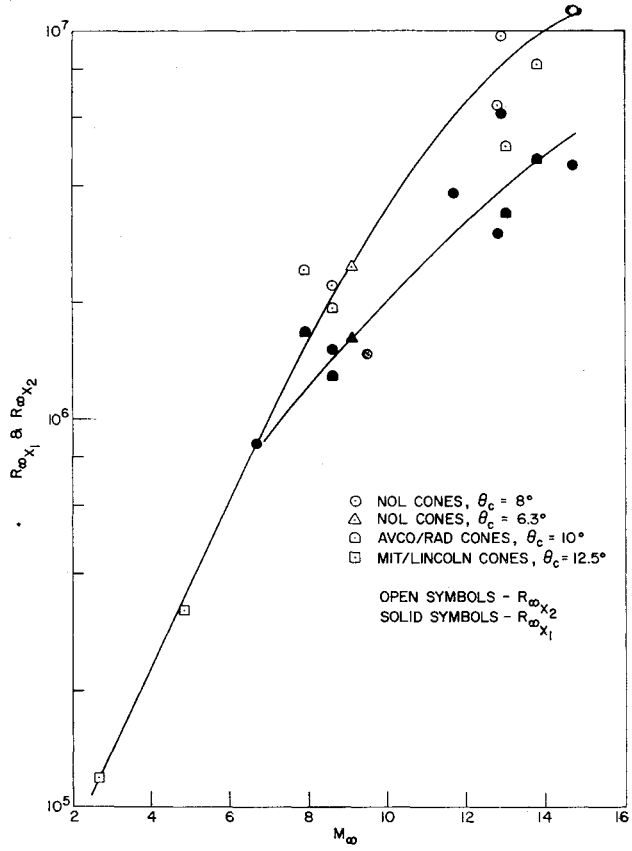

Fig. 16 Effect of freestream Mach number on wake transition Reynolds numbers.

From both the incipient transition and fully turbulent transition data correlations (Figs. 14 and 15) it appears that there exists a constant freestream wake transition Reynolds number independent of freestream body Reynolds number, but strongly influenced by the freestream Mach number. The existence of a constant transition Reynolds number independent of body diameter was mentioned by Lees[19] in his description of a hypersonic wake flow model. From a correlation of blunt-body wake transition data, Demetriades and Gold[20, 21] found a similar result.

The values of both wake transition Reynolds numbers $R_{\infty_{x_1}}$ and $R_{\infty_{x_2}}$ as a function of the flight Mach number are shown in Fig. 16. The solid symbols represent the incipient transition Reynolds numbers, and the open symbols represent the fully turbulent ones. It appears that the transition zone of the viscous core increases in length with an increase of the flight Mach number.

Conclusions

Hypersonic drag, stability, and wake characteristics for slender slightly blunted cones have been determined in a free-flight ballistics range.

The drag coefficients are linear functions of the mean squared angle of attack for constant values of flight Mach number and Reynolds number. The slope of these lines remains constant for different flight conditions and the lines are simply translated to give different values of C_{D_0}.

For fixed flight Mach number, the values of C_{D_0} can be correlated using a mean viscous interaction parameter $\bar{\chi}_M$. By assuming constant inviscid sharp cone pressure and by using a local Mach number distribution that exists because of slight nose bluntness, the values for C_{D_0} were theoretically predicted.

For values of the mean squared angle of attack up to 400 deg,[2] the static stability derivatives and the location of the center of pressure are essentially constant. This implies that the force and moment coefficients are linear functions of the angle of attack. For the preceding range of angle of attack, the static stability derivatives and locations of the center of pressure can be predicted using Newtonian impact theory.

With the possible exception of very small angles of attack, there do not appear to be viscous effects on the static stability characteristics of slender cones. At small angles of attack ($\overline{\alpha^2} < 10$) there appears to be a slight trend toward increased values of the stability derivatives and an aft movement of the center of pressure location.

In the region between 200 and 800 diam behind the body, the growth of the turbulent viscous core of the wake behind both cones and spheres is the same.

In the wake region between 20 and 800 diam behind cones and 200 and 800 diam behind spheres, the width of the turbulent viscous core is proportional to the cube root of (xC_DA). This constant of proportionality is a function of the flight Mach number.

Transition from laminar to turbulent flow in the viscous core of the wake behind slender cones can be described by freestream wake transition Reynolds numbers. Both the incipient and the fully turbulent wake transition Reynolds numbers appear to be independent of the freestream body Reynolds number for a constant Mach number, but strongly dependent upon the flight Mach number. The length of the transition zone increases with increasing flight Mach numbers.

References

[1] Hayes, W. D. and Probstein, R. F., "Viscous hypersonic similitude," J. Aerospace Sci. **26**, 815–824 (1959).

[2] Probstein, R. F., "Interacting hypersonic laminar boundary layer flow over a cone," Div. of Engineering, Brown Univ., TR AF2798/1 (March 1955).

[3] Probstein, R. F. and Elliott, D., "The transverse curvature effect in compressible axially symmetric laminar boundary layer flow," J. Aeronaut. Sci. **23**, 208–224, 236 (1956).

[4] Yasuhara, M., "Axisymmetric viscous flow past very slender bodies of revolution," J. Aerospace Sci. **29**, 667–679, 688 (1962).

[5] Wilkinson, D. B. and Harrington, S. A., "Hypersonic force, pressure and heat transfer investigations of sharp and blunt slender cones," Arnold Engineering Development Center, Tech. Doc. Rept. AEDC-TDR-63-177 (August 1963).

[6] Whitfield, J. D. and Griffith, B. J., "Hypersonic viscous drag effects on blunt slender cones," AIAA Preprint 63-434 (1963).

[7] Crogan, L. E., "Drag and stability data obtained from free-flight hypersonic firings of both pointed and blunt nosed 12°40′ total angle cones at several range pressures," Naval Ordnance Lab. TR63-36 (to be published).

[8] Lyons, W. C., Jr., Brady, J. J., and Levensteins, Z. J., "Hypersonic drag, stability, and wake data for cones and spheres," AIAA Preprint 64-44 (1964).

[9] Hayes, W. D. and Probstein, R. F., *Hypersonic Flow Theory* (Academic Press, New York, 1959), Chap. I, pp. 6–7.

[10] Wilson, R. E., "Laminar boundary-layer growth on slightly blunted cones at hypersonic speeds," J. Spacecraft Rockets (to be published).

[11] Chapman, D. R., "Laminar mixing of a compressible fluid," NACA TN 1800 (February 1949).

[12] Wilson, R. E., "Real gas laminar boundary layer skin friction and heat transfer," J. Aerospace Sci. **29**, 640–647 (1962).

[13] Wells, W. R. and Armstrong, W. O., "Tables of aerodynamic coefficients obtained from developed Newtonian expressions for complete and partial conic and spheric bodies at combined angles of attack and sideslip with some comparison with hypersonic experimental data," NASA TR-R-127 (1962).

[14] Anderson, J. D., Jr., "Hypersonic viscous flow over cones at nominal Mach 11 in air," Aeronautical Research Labs., Office of Aerospace Research, U. S. Air Force, Wright-Patterson Air Force Base, Ohio ARL 62-387 (July 1962).

[15] Townsend, A. A., *The Structure of Turbulent Shear Flow* (Cambridge University Press, Cambridge, England, 1956), Chap. VII, pp. 169–171.

[16] Slattery, R. E. and Clay, W. G., "The turbulent wake of hypersonic bodies," ARS Preprint 2673-62 (1962).

[17] Lykoudis, P. S., "The growth of the hypersonic turbulent wake behind blunt and slender bodies," The Rand Corp. Memo. RM-3270-PR (January 1963).

[18] Pallone, A. J., Erdos, I. I., Eckerman, J., and McKay, W., "Hypersonic laminar wakes and transition studies," AIAA Preprint 63-171 (1963).

[19] Lees, L., "Hypersonic wakes and trails," ARS Preprint 2662-62 (1962).

[20] Demetriades, A. and Gold, H., "Transition to turbulence in the hypersonic wake of blunt-bluff bodies," ARS J. **32**, 1420–1421 (1962).

[21] Demetriades, A. and Gold, H., "Correlation of blunt-bluff body wake transition data," Graduate Aeronautical Lab., California Institute of Technology Internal Memo. 12 (September 1962).

NOVEMBER 1964 AIAA JOURNAL VOL. 2, NO. 11

A Theoretical Study of the Inviscid Hypersonic Flow about a Conical Flat-Top Wing-Body Combination

PAUL MANDL*
National Research Council, Ottawa, Ontario, Canada

By combining the theory of linearized characteristics with the hypersonic small disturbance approximation, explicit expressions are derived for the shock shape, the flow field, the surface pressure distribution, and the aerodynamic forces for a delta wing and half-cone combination traveling at hypersonic speeds and small incidence. The theory is applied to a particular configuration for which surface pressure measurements are available. The theoretical and experimental pressure distributions agree quite closely on the body surface; but in the wing-body junction and on the wing, the theory predicts pressures that are too low.

Nomenclature

a = local speed of sound
b = total wing span
C_A = axial force coefficient
C_D = drag coefficient
C_L = lift coefficient
C_N = normal force coefficient
C_p = pressure coefficient $[(p - p_\infty)/\frac{1}{2}\rho_\infty U_c^2]$
c_v = specific heat at constant volume
g_{2n}, h_{2n}, j_{2n}, k_{2n} = Fourier coefficients
l = spanwise distance measured from windward generator
M_∞ = freestream Mach number
M_2 = flow Mach number perpendicular to leading edge
$\mathbf{n}$ = vector normal to shock surface
p = absolute pressure
$\mathbf{q}$ = fluid velocity vector
q = magnitude of fluid velocity
$\hat{q}$ = limit speed
R, θ, ϕ = spherical coordinates (Fig. 1)
S = specific entropy
s = nondimensional entropy
U_∞ = freestream velocity
u_{2n}, v_{2n}, w_{2n} = Fourier coefficient associated with fluid velocity
s_{2n} = Fourier coefficient associated with entropy distribution
α = incidence of configuration axis
γ = ratio of specific heats
δ = angle between shock normal and meridian plane
ϵ = density ratio across cone shock
θ_c = semiapex angle of cone
θ_s = local shock wave angle
λ = semiapex angle of wing
ρ = density
χ, = shock angle (Fig. 3)
χ' = angle between velocity perpendicular to leading edge and leading edge shock

Subscripts and Superscripts

∞ = freestream
e = region downstream of leading edge shock
0 = axially symmetric flow
b = body
w = wing

Received January 29, 1964; revision received May 28, 1964. A more detailed account of this research including further results is given in the National Aeronautical Establishment. Report LR-389. Acknowledgement is due to J. C. Basinski, who programed the final equations for the Bendix G-15 computer and did all the numerical work. The author would also like to thank the Director of the National Aeronautical Establishment for permission to publish this paper.

* Senior Research Officer, National Aeronautical Establishment.

1. Introduction

CURRENT interest in orbital gliders and lifting hypersonic vehicles has stimulated both theoretical and experimental work on the prediction of flow fields about such configurations. As a suitable aircraft design developing high lift-drag ratios in hypersonic flight, a flat-top wing-body combination has been proposed in Ref. 1. This configuration consists of a thin, highly swept delta wing beneath which is mounted a half conical body.

Although experimental data on flat-top configurations are being steadily accumulated, there exist relatively few theoretical studies of the flow about such shapes. A method for predicting the aerodynamic forces on flat-top configurations has been presented in Ref. 2. Since it is based on linear theory, its validity is necessarily restricted to the low supersonic speed range. In Ref. 3, a semiempirical method based on the inviscid conical flow equations has been devised for predicting the hypersonic flow about slender flat-top configurations. Although the agreement between the predicted and the experimental surface pressure distribution is remarkably good, the theory is in error because the calculated pressures on the wing do not reduce to those at zero incidence where they are known from the flow about the complete cone.

The purpose of the present investigation is to develop a rational theory of the flow about conical flat-top configurations